nature communications

Article

https://doi.org/10.1038/s41467-024-51268-y

Magnetostriction, piezomagnetism and domain nucleation in a Kagome antiferromagnet

Received: 15 February 2023

Accepted: 2 August 2024

Qingkai Meng[1], Jianting Dong[1], Pan Nie[1], Liangcai Xu[1], Jinhua Wang[1], Shan Jiang[1,2], Huakun Zuo[1], Jia Zhang[1], Xiaokang Li[1] ✉, Zengwei Zhu[1] ✉, Leon Balents[3,4] & Kamran Behnia[2] ✉

Whenever the elastic energy of a solid depends on magnetic field, there is a magnetostrictive response. Field-linear magnetostriction implies piezomagnetism and vice versa. Here, we show that Mn_3Sn, a non-collinear antiferromanget with Weyl nodes, hosts a large and almost perfectly linear magnetostriction even at room temperature. The longitudinal and transverse magnetostriction, with opposite signs and similar amplitude are restricted to the kagome planes and the out-of-plane response is negligibly small. By studying four different samples with different Mn:Sn ratios, we find a clear correlation between the linear magnetostriction, the spontaneous magnetization and the concentration of Sn vacancies. The recently reported piezomagnetic data fits in our picture. We show that linear magnetostriction and piezomagnetism are both driven by the field-induced in-plane twist of spins. A quantitative account of the experimental data requires the distortion of the spin texture by Sn vacancies. We find that the field-induced domain nucleation within the hysteresis loop corresponds to a phase transition. Within the hysteresis loop, a concomitant mesoscopic modulation of local strain and spin twist angles, leading to twisto-magnetic stripes, arises as a result of the competition between elastic and magnetic energies.

Following the discovery of a large room-temperature anomalous Hall effect (AHE) in Mn_3Sn[1] and in Mn_3Ge[2], this family of noncolinear antiferromagnets[3] became a subject of experimental[4–7] and theoretical[8–14] attention. The AHE signal is present at room temperature and can be inverted with a low magnetic field. Therefore, the discovery has a technological potential in the field of antiferromagnetic spintronics[15–19]. Very recently, Ikhlas et al.[20] reported that Mn_3Sn displays a large piezomagnetic effect at room temperature and the sign of the AHE can be modified by a sufficiently large uniaxial stress. By contrasting the response of magnetization and AHE, they demonstrated that the ultimate origin of the AHE is the residual Berry curvature. This confirmed a theoretical prediction[21], which argued that AHE in a non-collinear antiferromagnet does not require spontaneous magnetization.

Piezomagnetism, the generation of magnetic moment upon the application of strain, σ, is intimately linked to magnetostriction, ϵ, the field-induced contraction or elongation of the lattice[22]. Thermodynamics imposes a strict equivalence between the piezomagnetic response $(\frac{\partial M}{\partial \sigma})$ and the field slope of magnetostriction $(\frac{\partial \epsilon}{\partial B})$. Both quantities represent the second derivative of the free energy with

---

[1] Wuhan National High Magnetic Field Center and School of Physics, Huazhong University of Science and Technology, Wuhan 430074, China. [2] Laboratoire de Physique et d'Etude de Matériaux (CNRS), ESPCI Paris, PSL Research University, 75005 Paris, France. [3] Kavli Institute for Theoretical Physics, University of California Santa Barbara, Santa Barbara, CA 93106-4030, USA. [4] Canadian Institute for Advanced Research, Toronto, ON, Canada.
✉ e-mail: lixiaokang@hust.edu.cn; zengwei.zhu@hust.edu.cn; kamran.behnia@espci.fr

respect to magnetic field and stress ($\partial^2 F/\partial\sigma\partial B$) and their unavoidable equality is a specific case of Maxwell relations[23].

Magnetostriction, first discovered in ferromagnetic iron by Joule[24], is technologically attractive[25], because it can be used to conceive devices converting magnetic to mechanical energy and vice versa. Fundamentally, it arises when the magnetic field plays a role in setting the magnitude of the elastic energy. This can happen in metals[26] where it is delectably large (that is $>10^{-6}$ T^{-1})whenever the electronic density of states depends on magnetic field. Known cases include heavy-fermion systems near field-induced instabilities[27] and dilute metals subject to quantizing magnetic fields[28]. In ferromagnets, the dominant magnetostrictive response is due to field-induced displacement and rotation of magnetic domains and the boundary between them. When all domains align and magnetization saturates, magnetostriction collapses[29,30] (See also our data on cobalt below). In antiferromagnets, magnetostriction, drawing significant interest recently[20,31,32], is usually small and quadratic in magnetic field[33–35]. Save for a limited group of 35 antiferromagnetic classes (out of a total of 122 magnetic point groups), symmetry considerations forbid linear magnetostriction[33,36,37].

Here, we report on a detailed study of magnetostriction in Mn_3Sn, which belongs with a $mm'm'$ magnetic point group[12], not of the 35 antiferromagnetic classes allowing linear magnetostriction[33,36,37]). The linear magnetostriction is allowed by symmetry, because of the residual ferromagnetism.

By studying four different samples, we find that the slope of linear magnetostriction, Λ, and the spontaneous magnetization, M_0 both depend on the concentration of Sn vacancies. The dependence of Λ on Sn concentration allows us to reconcile the amplitude of the piezomagnetic coefficient resported by Ikhlas et al.[20], with our data.

We argue that the field-induced in-plane distortion of the spin texture and the competition between magnetic and elastic[38] energies leads to the emergence of linear magnetostriction. In this anti-chiral[39] spin texture, a magnetic field oriented along the kagome planes steadily twists the spins, as seen by torque magnetometry[40]. The field-induced rotation of spins generates an almost perfectly linear magnetostriction from 0.02 T to 9 T, which is to be contrasted with the magnetostriction caused by re-orientation of spins close to a ferromagnetic-antiferromagnetic phase boundary[41].

We also find that magnetostriction displays a discontinuous jump at the threshold magnetic field for domain nucleation. This is a signature of a second-order phase transition. The amplitude of the jump implies that, during the passage between single-domain regimes of opposite polarities, there are structural stripes with a mesoscopic width. We dub these stripes twisto-magnetic, since they refer to concomitant modulations of local strain and local spin orientation. Pinning down their structural details emerges as a subject for future experimental and theoretical studies.

Experimental

The single crystals used in this study were grown by the vertical Bridgman method, as detailed in the ref. 42. Mn_3Sn crystallizes into hexagonal DO_{19} structure. It is known that the single crystals are not stoichiometric and the Mn:Sn ratio is larger than 3[43]. As we will argue below, this is because a small fraction of Sn sites remain unoccupied and therefore the chemical formula becomes $Mn_3Sn_{1-\delta}$[44], with a number of physical properties depending on δ. The four samples, which were extensively studied this had different concentrations of Sn vacancies: $Mn_3Sn_{0.871}$ (#1), $Mn_3Sn_{0.891}$ (#2), $Mn_3Sn_{0.827}$ (C1) and $Mn_3Sn_{0.875}$ (C2). The samples dimensions were $0.82\times1.02\times1.42\ mm^3$ (#1), $1.01\times1.70\times2.05\ mm^3$ (#2), $0.93\times1.80\times4\ mm^3$ (C1) and $4\times0.5\times1.8\ mm^3$ (C2). Samples #1 and #2 were from one batch, while samples C1 and C2 were from another batch.

The dilatometer used in this study is sketched in Fig. 2a, b. It consists of two metallic plates forming a capacitor. One is kept still, while the other, to which the sample is clamped can move when the length of the sample changes. As the field is swept, this change gives rise to the variation of the capacitance between the two plates[45,46], which can be measured by a capacitance bridge. Please refer to the Methods section for more measurement details.

Results

Figure 1a, b shows the crystal and magnetic structure of Mn_3Sn. Each spin located on a Mn site is oriented 120 degrees off its adjacent spin on the same triangle in a kagome layer. This is an antichiral structure where the rigid clockwise rotation of the triangle with three spins on its vertices would lead to an anti-clockwise rotation of spins on each site[39]. The magnetic moment on each Mn site is ~3 Bohr magnetons, μ_B. However, the net magnetic moment is only ~0.002–0.003 μ_B per Mn atom, indicating almost total compensation between moments oriented 120-degree off each other. This inverse triangular spin structure emerges below $T_N = 420$ K[1,3] and is destroyed below a temperature, which can be tuned by changing the Mn:Sn ratio.[1,3,4].

Zero-field thermal expansion

Figure 1c shows the thermal expansion data along the three crystal-axis orientations in sample #1. The thermal expansion coefficient is positive along the three orientations. It is larger in the kagome planes and there is a modest anisotropy which decreases with warming. Our thermal expansion data is agreement with the results of a previous study restricted to temperatures above 200 K[47]. In Fig. 1c, for each orientation, the length at 2 K is taken as the reference. The inset of the Fig. 1c shows the thermal expansion coefficients at low temperatures. The destruction of the inverse triangular spin state around 50 K, indexed by a dashed line, does not cause any detectable anomaly.

Longitudinal and transverse magnetostriction

Figure 2c compares the longitudinal magnetostriction along the three crystalline orientations in low fields up to 0.3 T at 200 K. In our convention, ϵ_j^i refers to the magnetostriction measured along j when the magnetic field is along i. Longitudinal magnetostriction is contractile, and almost identical along the x and y axes. On the other hand, when the field is along the z-axis, there is no detectable signal. Figure 2d shows the magnetization in the same sample. There is a finite spontaneous magnetization for the two in-plane configurations, but not for the out-of-plane one. Magnetization has a finite slope along the three orientations, as reported previously[1]. The absence of out-of-plane longitudinal magnetostriction implies that uni-axial stress along z-axis does not affect out-of-plane magnetization. In contrast, the in-plane longitudinal magnetostriction is finite, implying that in-plane stress would affect the magnetization. Moreover, since the magnetostriction is linear in magnetic field, stress should shift magnetization without changing its slope as a function of magnetic field. This is indeed what was found by the recent study of piezomagnetism[20].

As seen in Fig. 2c, d, magnetostriction and magnetization behave concomitantly. When the magnetic field exceeds a critical threshold ($B_0 = 0.02$ T marked by two dashed vertical lines for the two sweeping orientations), magnetostriction peaks and magnetization starts to increase. B_0 is the field at which domains (with a polarity set by magnetic field and inverse to the prevailing one) nucleate. When the magnetic field exceeds a much larger amplitude (≈0.2 T), the system becomes single domain again[42]. We will discuss what happens when $B = B_0$, in more detail later below.

Figure 3a–d shows the longitudinal and the transverse magnetostriction for both x and y orientations at various temperatures. For both orientations, longitudinal magnetostriction is contractile and transverse magnetostriction is expansive. As seen from the figures, it is linear in all four configurations. The field slope of $\frac{\partial\epsilon}{\partial B}$ is extracted from this data and is plotted as a function of temperature in Fig. 3e, f. For all

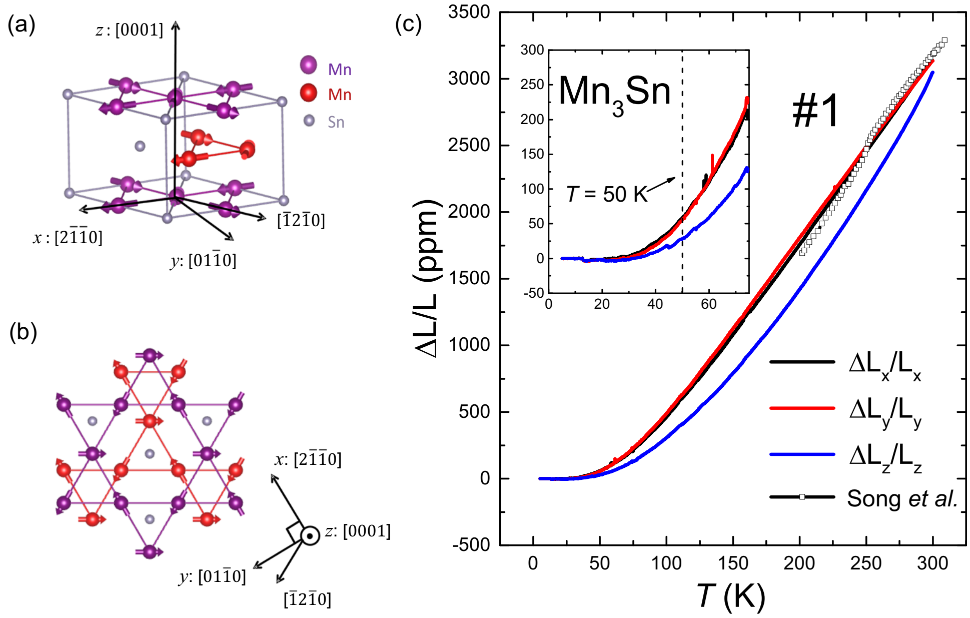

Fig. 1 | The magnetic structure and thermal expansion in Mn_3Sn. The spin-structure of Mn_3Sn, two layers of kagome structure of manganese (**a**), the Mn atoms in a triangular spin texture rotate 120 degrees (**b**). The axes called x, y and z axes refer to the $[2\bar{1}\bar{1}0]$, $[01\bar{1}0]$ and [0001] crystalline orientations. **c** Thermal expansion along three orientations for Mn_3Sn comparing to the result of Song et al.[47]. The inset shows the thermal expansion responses at low temperatures. The destruction of the inverse triangular spin state indexed by a dashed line, does not cause a detectable anomaly.

four configurations, $\frac{\partial \epsilon}{\partial B}$ are flat above 150 K and begin to increase with decreasing temperature with the approach of the 50 K phase transition (for a brief glimpse to the magnetostriction below 50K, see Supplementary Fig. 11 in the supplementary materials[48]).

We conclude that even at room temperature, for both x and y directions, there is a large longitudinal $\frac{\partial \epsilon}{\partial B}$ of comparable magnitude ($\approx -1.5 \times 10^{-5}\ T^{-1}$) slightly larger than a transverse signal of opposite sign ($\approx +1.1 \times 10^{-5}\ T^{-1}$). We also measured transverse magnetostriction for other configurations and found a tiny response within the margin of our experimental resolution (see Supplementary Fig. 3 in the supplementary materials[48]).

Linear magnetostriction up to 9 T

Figure 4a illustrates the evolution of magnetostriction up to 9 T. One can express the magnetostriction as the sum of a linear and a quadratic term : $\epsilon = a_l B + a_q B^2$. Table 1 lists the best fits to these coefficients for two different samples.

The combination of a dominant linear (a_l) and a sub-dominant quadratic (a_q) term up to ≈ 9 T is reminiscent of the case of UO_2 in its magnetically ordered state[32]. Interestingly, the amplitude of the linear magnetostriction is roughly similar in the two cases ($\approx 10^{-5}\ T^{-1}$). However, here it is a room-temperature phenomenon, while in UO_2 it emerges below a Néel temperature of 30 K[32]. No saturation is visible in our data up to 9 T in contrast with what is observed in ferromagnets (For an example, see the case of Co in the supplementary materials[48]). Figure 4b shows a sketch of mechanism. We will discuss the microscopic origin of this robust field-linear magnetostriction in the next section.

Discontinuity at the threshold of domain nucleation

Figure 5a, b is a zoom on the low-field behavior near B_0. One can see a discontinuity in longitudinal magnetostriction at $B_0 \approx 0.02$ T. This is the field at which magnetic domains nucleate. When the magnetic field is swept down to zero, the magnetostriction linearly decreases to a null value. It changes sign with the inversion of the magnetic field. But the magnetization and the anomalous Hall effect do not change sign when the magnetic field inverts. They continue to have a sign opposite to the magnetic field. At B_0, both the magnetization and the AHE begin to evolve along the orientation imposed by the magnetic field[42]. At this field, longitudinal magnetostriction shows a discontinuous jump (Fig. 5a, b), in contrast with the weaker anomaly seen in transverse magnetostriction. The observed jump represents a discontinuity in the second derivative of the free energy and implies a second-order phase transition.

The magnetostriction hysteresis loop in Mn_3Sn differs qualitatively from other cases of linear magnetostriction such as MnF_2 or UO_2, where the response is set by domain rotation (see Supplementary Fig. 6 in the supplementary materials[48]). We will come back to the implications of this observation and also the Fig. 5e, f in the next section.

Multiplying the amplitude of the jump in magnetostriction by the Young Modulus ($E = 123$ GPa[38]) allows to quantify the change in elastic energy, shown in the Fig. 5c. Similarly, we can identify the energy cost of domain nucleation with the product of B_0 and magnetization, shown in the Fig. 5d. The two energies differ by more than three orders of magnitudes and both tend to vanish at $T_N = 420$ K as expected.

Sample dependence

Having found that the amplitude of linear magnetostriction differs from one sample to the other, we undertook an extensive examination of magnetization and magnetostriction of additional samples. Figure 6a portrays the magnetization of several samples at 300K. In addition to four different samples used in our study, the figure includes the sample studied by Ikhlas et al. in their piezomagnetic study[20]. One can see that the amplitude of the jump in magnetization, M_0 varies from sample to sample.

Figure 6b plots the amplitude of this spontaneous magnetization as a function of δ, the concentration of Sn vacancies. In addition to our samples, we include three samples studied by Kurosawa et al.[49]. There is a clear correlation between the amplitude of M_0 and δ. This implies that in-plane ferromagnetism is, at least partially, caused by the presence of Sn vacancies.

Figure 6c compares the magnetostriction of four different samples. There is a visible difference in slope of ϵ_x^x. In other words, linear

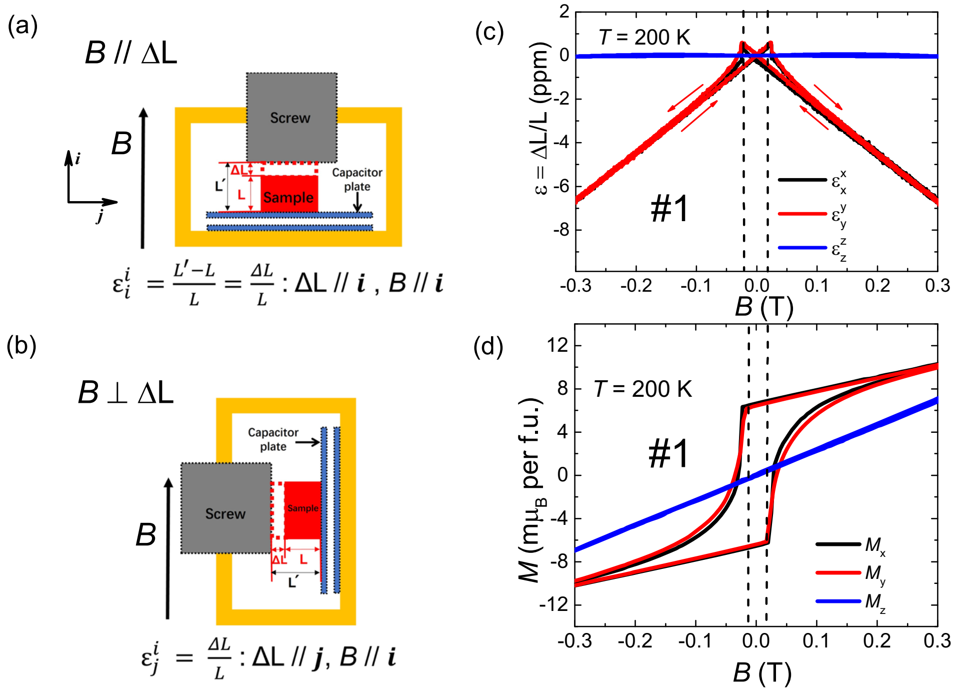

Fig. 2 | The magnetostriction in Mn_3Sn. a, **b** The setup to measure longitudinal and transverse magnetostriction. The magnetostriction was measured by the capacitance between two metallic plates. The length change of the clamped sample leads to the change of the distance between the plates, and therefore the capacitance. **c**, **d** Longitudinal magnetostriction (top) and magnetization (bottom) as a function of the magnetic field for three crystalline orientations. The in-plane magnetostriction ($B \,//\, x, y$) is large, but for out of plane orientation ($B \,//\, z$), it is negligible. Magnetization displays the same slope for the three orientations. Dashed vertical lines indicate the threshold fields for domain inversion.

magnetostriction has not the same amplitude. Plotting $\Lambda = \frac{\partial}{\partial B}\epsilon_x^x$ as a function of M_0 (Fig. 6d) of the four crystals shows a clear quasi-linear correlation between the two. The figure includes another data point, Λ reported by the piezomagnetic study[20]. Thus, residual ferromagnetism is not only indispensable for the existence of linear magnetostriction, but also sets its amplitude. As seen in Supplementary Fig. 12[48], the presence of Sn vacancies leads to a detectable change in the lattice parameter along the *a*-axis. Along the *c*-axis, the variation is undetectably small. Note that the difference in lattice parameter among the samples is at least an order of magnitude larger than the change induced by a 10 T magnetic field in each sample.

Discussion

Origin of the linear magnetostriction

Both piezomagnetism and magnetostriction arise because any deviation of the elementary units of Mn_3Sn from a perfect equilateral geometry disrupts the cancellation of the net moment of the three spins therein. Microscopically, strain transforms the equilateral triangle to an isosceles one. The cancellation is spoiled because the two most nearby spins have a stronger antiferromagnetic coupling, and hence twist slightly toward a more antiparallel alignment. Consequently, a distortion of the triangle induces a net moment (piezomagnetism), and a net moment caused by field-induced twisting of the spins[39,40] induces a distortion (magnetostriction).

In the ideal system, where all triangles are identical, one can understand this effect very simply from both a microscopic calculation and a symmetry point of view. In this case, we can consider the spins on a single triangle, and define three linear combinations:

$$\begin{aligned} \boldsymbol{M} &= S_0 + S_1 + \boldsymbol{S}_2, \\ \boldsymbol{\Phi} &= S_0 + e^{-2\pi i/3} S_1 + e^{-4\pi i/3} S_2, \end{aligned} \tag{1}$$

Here, $\boldsymbol{M}$ is a real vector representing the total spin on a triangle, and $\boldsymbol{\Phi}$ is a complex vector which defines the antiferromagnetic order parameter. For spins of fixed length S, we have $|\boldsymbol{M}|^2 + 2\boldsymbol{\Phi}^* \cdot \boldsymbol{\Phi} = 9S^2$. When the three spins are at 120 degrees to one another, $\boldsymbol{M} = 0$ and $\boldsymbol{\Phi}^* \cdot \boldsymbol{\Phi} = \frac{9}{2}S^2$. Note that when all spins rotate by 180 degrees, $\boldsymbol{\Phi}$ changes sign, but keeps its absolute value.

Nearest-neighbor exchange in these variables becomes

$$J(\boldsymbol{S}_0 \cdot \boldsymbol{S}_1 + \boldsymbol{S}_1 \cdot \boldsymbol{S}_2 + \boldsymbol{S}_2 \cdot \boldsymbol{S}_0) = \frac{J}{3}\left(|\boldsymbol{M}|^2 - \boldsymbol{\Phi}^* \cdot \boldsymbol{\Phi}\right). \tag{2}$$

One can see readily this favors the antiferromagnetic state. Now we include the simplest exchange-striction effect, which corresponds to the modification of the exchange J on a bond proportional to the change in its length. This is modeled by the term

$$H_{e-s} = -\sum_n Jg\left(\hat{\boldsymbol{f}}_n \cdot \boldsymbol{\varepsilon} \cdot \hat{\boldsymbol{f}}_n\right) \boldsymbol{S}_n \cdot \boldsymbol{S}_{n+1}, \tag{3}$$

where $\boldsymbol{S}_3 = \boldsymbol{S}_0$, $\boldsymbol{\varepsilon}$ is the strain tensor, and $\hat{\boldsymbol{f}}_n$ is the unit vector along the bond connecting spin n and $n+1$, and g is proportional to $-\frac{r}{J}\frac{dJ}{dr}$. Using Eq. (1), one obtains, dropping a trivial volume expansion contribution,

$$H_{e-s} = -\frac{Jg}{3} \mathrm{Re}\left[\varepsilon_+ (\boldsymbol{M} \cdot \boldsymbol{\Phi}^* - \boldsymbol{\Phi} \cdot \boldsymbol{\Phi})\right], \tag{4}$$

where $\varepsilon_+ = \frac{1}{2}(\epsilon_{xx} - \epsilon_{yy} + 2i\epsilon_{xy})$.

In a pure spiral state (either chiral or antichiral), the $\boldsymbol{\Phi} \cdot \boldsymbol{\Phi} = 0$ term vanishes. The remaining term in Eq. (4) describes an in-plane anisotropic stress arising in the presence of magnetization and antiferromagnetic order. The stress (and consequent strain) is induced *without spin-orbit coupling*, because the antiferromagnet order itself couples spin and orbital symmetries. Specifically, a 120 degree ordered state breaks both spin rotation and C_3 spatial rotation symmetries, but preserves the combination of the two – in the anti-chiral case, the two rotations are made in the opposite sense. One might think of the

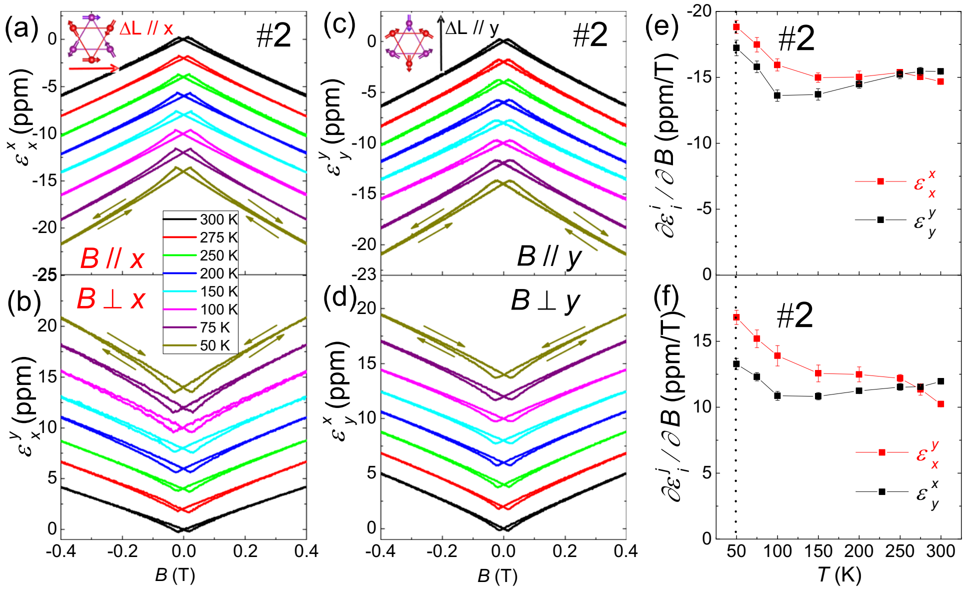

Fig. 3 | Longitudinal and transverse magnetostriction for two orientations. The longitudinal and transverse magnetostriction for $\Delta L//x$ (**a**, **b**) and $\Delta L//y$ (**c**, **d**) at various temperatures. **e**, **f** The temperature dependence of the slope of the magnetostriction: $(\frac{\partial\epsilon}{\partial B})$ for the four configurations. The vertical line marks the destruction of the anti-chiral magnetic order at 50 K. Note the opposite signs of the longitudinal and transverse responses.

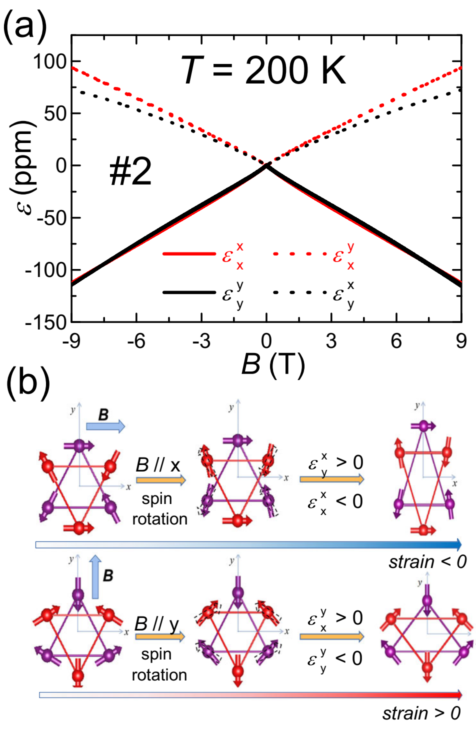

Fig. 4 | High-field magnetostriction and the mechanism. a Magnetostriction up to 9 T for four configurations. The nearly perfect linearity persists as the field is increased. **b** A sketch of the mechanism. When the field is applied along the x − or y − axes, the spin texture is distorted. Because of the spin-lattice coupling, the distortion of the spin angles leads to (a much milder) distortion of atomic bonds.

antiferromagnet itself as a state in which spin-orbit coupling is generated spontaneously!

To understand how this effect arises without SOC, we need to think about the presence of both magnetization and AF order. In Mn_3Sn, the AF order is long-range and well-established at room temperature. When we think about any single triangle of spins, the AF order parameter $\mathbf{\Phi}$ is therefore imposed upon it by other triangles coupled to it, and related to the order far away. Supposing this global AF order is somehow pinned (typically by an applied field), then the spin orientations on the triangle in question are almost fixed. If a small uniform magnetization is imposed, the spins rotate slightly, and then in turn leads to a difference of bond energies, which depends on the relative orientation of the AF order and the magnetization. That relative orientation determines the axes for the anisotropic stress, which will induce a strain that seeks to strengthen the exchange on the bond with the most anti-aligned pair of spins.

While this effect does not require SOC, other effects can occur when SOC is present. To allow for all possibilities, we consider the general form of linear couplings of an anisotropic in-plane strain ε_+ to the magnetic order parameters. Here we specialize to the *anti*-chiral state, whose order parameter is the complex *scalar* $\Phi = \Phi_x - i\Phi_y$. We assume $\Phi_z = \Phi_x + i\Phi_y = 0$, so there is pure anti-chiral order. We also express the in-plane magnetization as a second complex scalar $M = M_x - iM_y$. Then the most general free energy density linear in ε_+ is

$$f^{\rm gen}_{e-s} = -\,\mathrm{Re}\left[\epsilon_+\left(\gamma_1 M\Phi^* + \gamma_2 M^2 + \gamma_3(\Phi^*)^2\right)\right], \qquad (5)$$

where $\gamma_{1,2,3}$ are phenomenological coupling constants. By comparing to Eq. (4), we can see that $\gamma_1 = \frac{gJ}{3v_{\rm u.c.}}$, where $v_{\rm u.c.}$ is the volume per unit cell used to convert to an energy density. The other two couplings γ_2, γ_3 are zero in the absence of SOC, but are generally present and can be obtained for example from single ion anisotropy (SIA)[20].

Using the equations of elasticity, we have $\boldsymbol{\varepsilon} = \boldsymbol{C}^{-1}\boldsymbol{\sigma}$, where $\boldsymbol{\sigma} = -\partial f_{e-s}/\partial\boldsymbol{\varepsilon}$ is the strain induced by the spin-lattice coupling. For the case of polar anisotropy and a three-fold rotation axis along z, we find

$$\epsilon_+ = \frac{1}{2C_{66}}\left(\gamma_1 M^*\Phi + \gamma_2 (M^*)^2 + \gamma_3\Phi^2\right), \qquad (6)$$

where C_{66} is the shear modulus in Voigt notation. For fields which are larger than the hysteresis field, but still small enough that the magnetization is small, one can approximate $M \approx M_s + \chi H$, and $\Phi \sim |\Phi|\hat{H}^*$,

Table 1 | Parameters extracted by fitting the field dependence of the magnetostriction up to 9 T at 200 K for two samples

Sample	ϵ_x^x		ϵ_x^y		ϵ_y^y		ϵ_y^x	
	a_l	a_q	a_l	a_q	a_l	a_q	a_l	a_q
#1	-1.949	-0.0015	0.612	0.0004	-2.244	0.0156	1.091	0.0012
#2	-1.297	0.007	1.105	-0.0095	-1.174	-0.0092	1.021	-0.0252

The fitting parameters a_l and a_q were obtained by fitting the data to $\epsilon = a_l B + a_q B^2$. The units of a_l and a_q are $\times 10^{-5}$ T^{-1} and $\times 10^{-5}$ T^{-2}, respectively. The linear magnetostriction, Λ corresponds to a_l. One can see it totally dominates the quadratic term, even at the order of 10 T, $a_l \gg a_q \times B$.

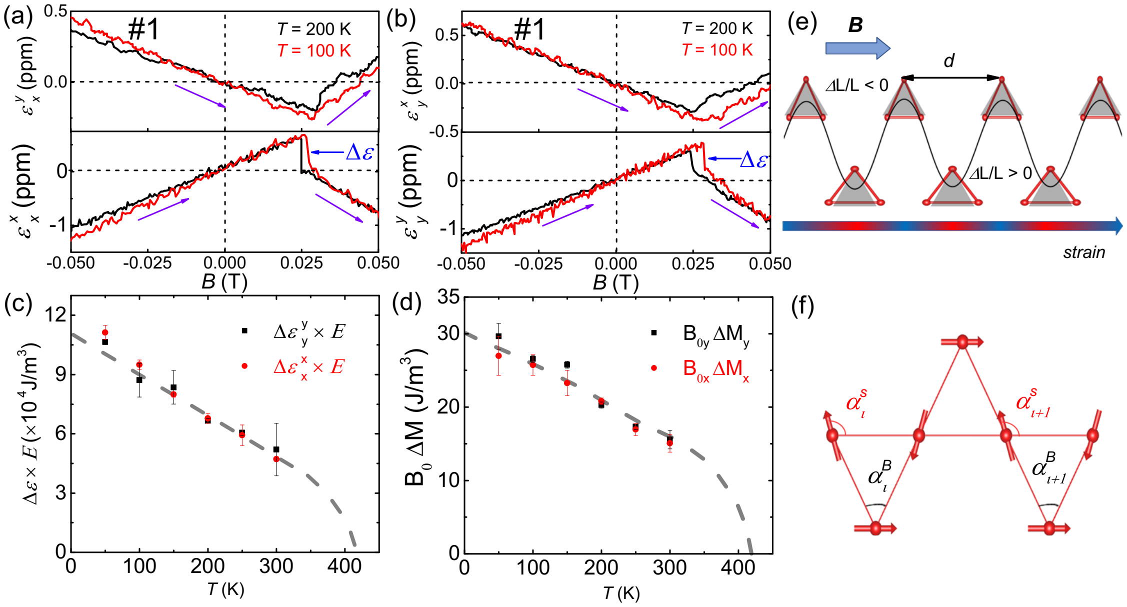

Fig. 5 | Discontinuity in a second-order derivative of the free energy. **a** Transverse and longitudinal magnetostriction for $\Delta L \,//\, x$. **b** Transverse and longitudinal magnetostriction for $\Delta L \,//\, y$. In both cases, the longitudinal magnetostriction shows a discontinuity at B_0. The two vertical dashed lines show the amplitude of magnetostriction because of the domain reversal. **c** The amplitude of this jump multiplied by the Young Modulus ($E = 123$ GPa) as a function of temperature. This quantifies the elastic energy associated with the jump. **d** The product of B_0 and magnetization as a function of temperature. This quantifies the energy cost of domain nucleation. The two energies differ in amplitude by more than three order of magnitudes. But, both tend to vanish at $T_N = 420$ K. **e** The sketch of modulation in space at B_0: Since $\epsilon(B = B_0) = \epsilon(B = 0)$, the overall magnetostriction should be zero with peaks of positive magnetostriction and valleys of negative magnetostriction, separated by a distance, d, much longer than the lattice parameter. **f** The sketch of two neighboring atomic triangles. If the difference in spins' angles (α_i^s) becomes much larger than the difference in the atomic bond's angle (α_i^B), then the gradient of magnetization is large enough to compensate the mechanical force due to a gradient in elastic energy.

where $H = H_x - iH_y$ and $\hat{H} = H/|H|$. We then have

$$\epsilon_+ \approx \frac{1}{2C_{66}}\left(\gamma_1|\Phi|M_s^*\hat{H}^* + \gamma_2\left(M_s^*\right)^2 + \gamma_3|\Phi|^2\left(\hat{H}^*\right)^2\right) + \frac{\chi}{2C_{66}}\left(\gamma_1|\Phi|\hat{H}^* + 2\gamma_2 M_s^*\right)H^* + O(H^2). \tag{7}$$

The second line describes linear in field magnetostriction:

$$\frac{d\epsilon_+}{dH^*} \approx \frac{\chi}{2C_{66}}\left(\gamma_1|\Phi|\hat{H}^* + 2\gamma_2 M_s^*\right) \tag{8}$$

We see that it arises from two contributions. The “intrinsic” term obtained above gives γ_1, which is independent of the spontaneous magnetization M_s. By contrast, the “extrinsic” term γ_2 gives a linear contribution proportional to $|M_s|$.

Consistency with the experiment would be achieved if γ_2 were the dominant contribution. This is surprising and in disagreement with naïve expectations, and $\gamma_2 \ll \gamma_1$ for the uniform system in the weak anisotropy limit. It seems that non-stoichiometry has the effect of dramatically enhancing γ_2.

Neumann’s principle

From a symmetry point of view, linear magnetostriction may occur in certain antiferromagnetic point groups[33], but occurs generically in ferromagnets. While Mn_3Sn is dominated by antiferromagnetism, it is in the symmetry sense a ferromagnet: it belongs to the ferromagnetic point group $mm'm'$ (see the supplementary materials[48]). Consequently, both a spontaneous zero field magnetization and magnetostriction are generically expected – neither are prohibited by Neumann’s principle. The ferromagnetism in Mn_3Sn is weak, however, because of the weakness of SIA. This enables the linear magnetostriction to extend over a very wide field range, simply because of the extended linearity of the magnetization due in turn to the large antiferromagnetic exchange J. Nevertheless, it is to be expected that residual ferromagnetism accompanies the presence of Λ.

Piezomagnetism and linear magnetostriction

Our magnetostriction data should match the piezomagnetic data[20]. Maxwell relations imply a thermodynamic identity between the results of two probes[29]:

$$\left(\frac{d\epsilon}{dH}\right)_\sigma = \left(\frac{dM}{d\sigma}\right)_H \tag{9}$$

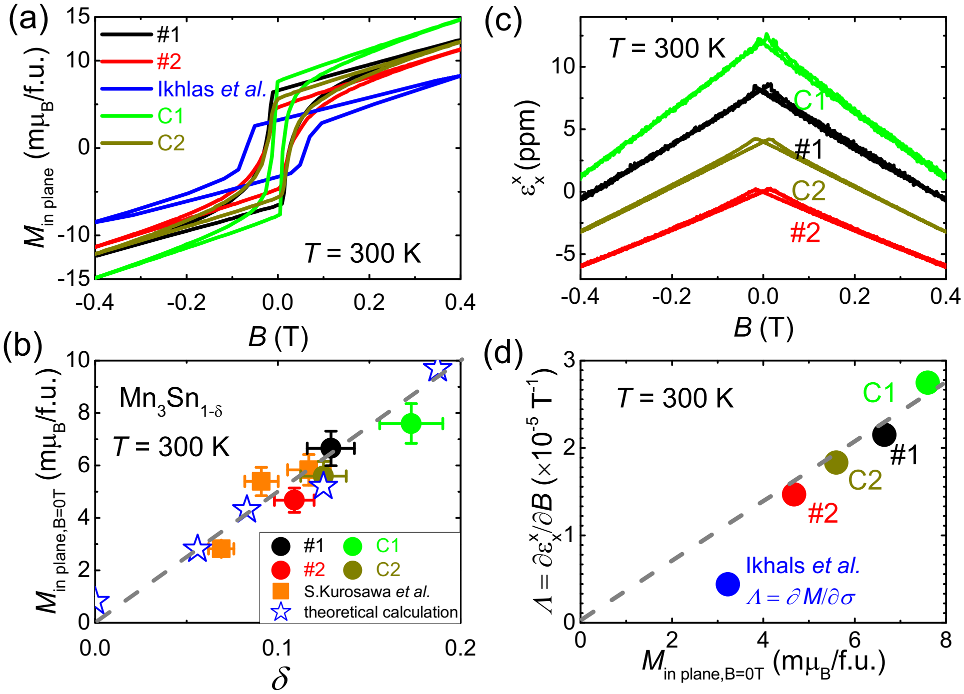

Fig. 6 | Amplitude of magnetostriction and magnetization and its correlation with the concentration of Sn vacancies. a Magnetization of different samples at 300 K. **b** The amplitude of the spontaneous magnetization as a function of the concentration of Sn vacancies in our samples and those reported in ref. **c** Magnetostriction of our samples at 300 K. **d** Λ as a function of spontaneous magnetization in our samples and the one reported by Ikhlas et al.[20] at 300 K.

The left hand side is the slope of field-linear magnetostriction and the right hand side is the piezomagnetic coefficient. Both represent the components of the same third-rank tensor Λ_{ijk}[22]. Measuring the stress dependence of magnetization, Ikhlas et al.[20] reported that $\frac{dM}{d\sigma} \simeq -0.055\,\text{Gauss MPa}^{-1}$ for the x-axis orientation (and slightly smaller in another sample along the y-direction). Now, magnetization in S.I. units is expressed in A/m and their results corresponds to $\frac{dM}{d\sigma} \simeq -4.4\times10^{-6}$ T^{-1} in S. I. units. This is significantly smaller that what we found in four different samples for both longitudinal and transverse magnetostriction. The absolute amplitude of $\frac{\partial\epsilon}{\partial B}$ was always larger than 1×10^{-5} T^{-1}).

However, as seen in Fig. 6d the discrepancy fades away by considering the fact that the spontaneous magnetization in the sample subject to the piezomagnetic study was smaller than our samples, indicating that its stoichiometry was different from ours. The calculated piezomagnetic coefficient of Mn$_3$Sn$_{1-\delta}$ is in the same order of magnitude as the experimental results(see Supplementary Fig. 10 in the supplementary materials[48]). However, any quantitative account of Λ should explain the linear proportionality between piezomagnetic/magnetostrictive response and the spontaneous magnetization remains unexplained. This requires to consider the role of Sn vacancies.

Unoccupied Sn vacancy sites

Mn$_3$Sn crystal have a deficit of Sn atoms[43,44]. A number of Sn sites are vacant. As seen in Fig. 6b, the amplitude of spontaneous magnetization increases with increasing density of these Sn vacancies. Moreover, the spontaneous magnetization calculated by first-principle theory can be perfectly matched with our experimental data. In contrast, if vacant Sn sites were occupied by Mn atoms (giving rise to a chemical formula of Mn$_{3+x}$Sn$_{1-x}$) the calculated spontaneous magnetization is two orders of magnitude larger than the experimental data (see Supplementary Fig. 9 in the supplementary materials[48]). Note that this calculation was performed for T= 0 K (See More Computational Details in the supplementary materials[48])). The agreement between theory and experiment leads to conclude that the chemical formula is Mn$_3$Sn$_{1-\delta}$.

One expects two important effects introduced by these Sn vacancy sites. First, they disrupt the local antiferromagnetic spin cancellation, and induce spin twisting and a local magnetic moment (Fig. 7). Second, they break the high symmetry of the nearby Mn clusters, which may change the orbital character of these moments, enhancing spin-orbit effects and SIA. These two effect provide a basis for understanding the observed trends. Spontaneous magnetization increases with non-stoichiometry because each Sn vacancy brings an uncompensated moment. The coupling γ_2, which was shown in Eq. (7) to drive to $\Lambda \propto M_s$, can only arise from enhanced SIA. These observations are strongly suggestive. A quantitative account of Λ in this picture, requires a Hamiltonian for the non-stoichiometric compound, a substantial theoretical effort, beyond the scope of the present work.

Twisto-magnetic stripes

In the previous section, we saw that at a small field of $B \simeq 0.02$ T, longitudinal magnetostriction shows a discontinuous drop but the transverse magnetization shows just a peak. At this field, the spontaneous magnetization begins to change sign, signaling that the sample is no more single domain[42,50]. The accumulated magnetic energy (i.e. the product of magnetization and magnetic field) at B_0 becomes sufficiently large to pay the energy cost of building domain walls.

As seen in Fig. 5a, b, at $B = B_0$, longitudinal magnetostriction falls to zero. The total volume of the sample is therefore occupied by magnetic domains whose mutual mechanical deformation along the orientation of the magnetic field cancel each other. Since the total magnetization is not zero at B_0, the multi-domain regime, restricted to a field window between 0.02 T to 0.2 T, there should be a concomitant modulation of lattice parameter and spin orientation (Fig. 5e) at Mn sites. When two neighboring atomic triangles have slightly different lattice parameters, atomic-bond angles and spin twisted angles, the

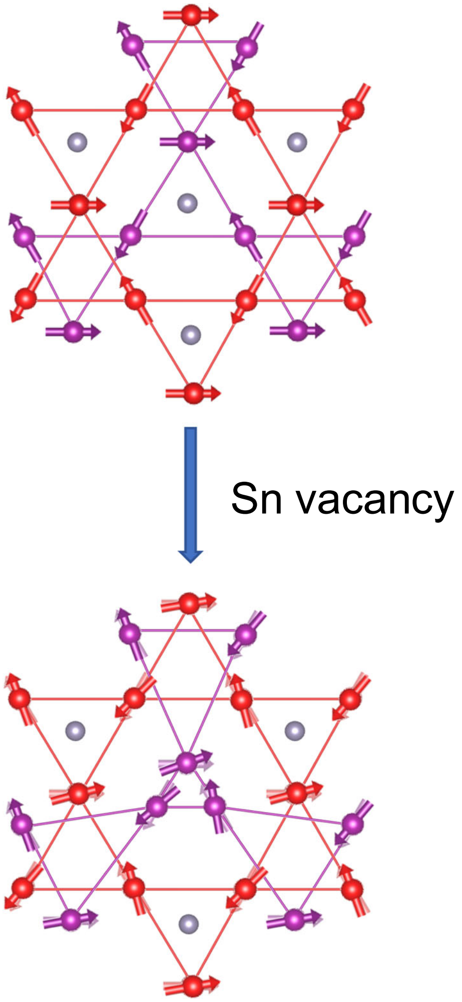

Fig. 7 | Possible outcome of a Sn vacancy. The vacancy of Sn atoms may generate residual ferromagnetism by twisting the spins of neighboring regular Mn atoms.

Table 2 | Λ_{ij} in several magnetically-ordered solids

Materials	Λ_{ij} (10^{-6} T^{-1})	T (K)	PM or LM	Refs
CoF_2	$\Lambda_{14} = 21$	20	PM	54
	$\Lambda_{36} = 8.2$	20	PM	54
	$\Lambda_{36} = 9.8$	4	LM	54
MnF_2	$\Lambda_{14} = 0.2$	20	PM	54
	$\Lambda_{36} = 0.07$	60	PM	55
$DyFeO_3$	$\Lambda_{36} = 6$	6	LM	54
$YFeO_3$	$\Lambda_{15} = 1.7$	6	LM	54
$YCrO_3$	$\Lambda_{15} = 1$	6	LM	54
Terfenol-D	$\Lambda_{11} = 4000$	300	LM	56
α-Fe_2O_3	$\Lambda_{22} = 3.2$	77	PM	54
	$\Lambda_{22} = 1.9$	78	LM	54
	$\Lambda_{22} = 1.3$	100	LM	54
	$\Lambda_{14} = 1.7$	77	PM	54
	$\Lambda_{14} = 0.3$	78	LM	54
	$\Lambda_{14} = 0.9$	10	LM	54
UO_2	$\Lambda_{14} = 10.5$	2.5	LM	32
$Mn_3Sn_{1-\delta}$	$\Lambda_{11} = 4.4$	300	PM	20
	$\Lambda_{22} = 3.8$	300	PM	20
$Mn_3Sn_{0.891}$	$\Lambda_{11} = 14.6$	300	LM	This work
	$\Lambda_{22} = 15.4$	300	LM	This work
	$\Lambda_{12} = 11.1$	300	LM	This work

Note the limited range of variety in amplitude among solids with different ordering temperatures. Note also that there are cases of discrepancy between measurements of piezomagnetism and magnetostriction.

force exerted by the strain gradient will be compensated by the magnetic force due to the angle between twisted spins (see Fig. 5f). Given that the magnetic energy density (that is the product of magnetization and magnetic field) is only a few pascals[42]), which is orders of magnitude smaller than the elastic energy density, the differential angle of neighboring spins should be orders of magnitude larger than the differential angle of neighboring atomic bonds. A magnetic field of 13T can distort the spin structure by around two degrees[40]. This intricate mesoscopic structure emerges as a subject of futures investigation by experimental probes in both real space and in momentum space.

Comparison with other magnets

Table 2 lists solids in which linear magnetostriction and piezomagnetism have been observed[22]. We saw that in the case of Mn_3Sn, the departure from stoichiometry plays a crucial rule in setting the amplitude of Λ. Notice the discrepancy in the reported amplitudes of linear magnetostriction and piezomagnetism in other cases, which is yet to be sorted out. Measuring the same sample with both methods could settle the issue.

In summary, we find that Mn_3Sn hosts a large in-plane magnetostriction dominantly linear in magnetic field. We argue that it arises from the field-induced twist of spins and its amplitude can be accounted for given the magnetic and the elastic energy scales. Thermodynamic consistency between the magnetostriction and the piezomagnetic data is achieved only by considering the fact that both, as well as spontaneous magnetization depend on the concentration of Sn vacancies. The sudden vanishing of longitudinal magnetostriction at the onset of domain nucleation implies the existence of twisto-magnetic stripes with a concomitant modulation of strain and local magnetization in a narrow field window.

Methods

Sample

The Mn_3Sn single crystals used in this work were grown using the vertical Bridgman method[42]. The millimeter-size samples were cut from the as-grown samples by a wire saw.

Crystal orientations were determined by a single crystal XRD diffractometer (XtaLAB mini II of Rigaku). The variation of temperature during magnetostriction measurements remained within 0.05%.

Measurement

A capacitive dilatometer with a resolution of ΔL = 0.02 Å made by Innovative Measurement Technology was used to measure magnetostriction in an Oxford Instruments Teslatron PT. We used an Andeen-Hagerling 2550A capacitance bridge for our measurements. By installing the dilatometer perpendicular to the magnetic field, we also measured magnetostriction in the transverse configuration. The reliability of our set-up was checked by measuring magnetostriction in a cobalt single crystal (see the supplementary materials[48]).

Calculation

The theoretical computation was realized by first principles calculations using Vienna ab initio simulation package (VASP)[51] with the projector augmented wave (PAW) pseudopotential[52] and the Perdew-Burke-Ernzerhof (PBE) type of the generalized gradient approximation (GGA) of the exchange correlation potential[53]. See More Computational Details in the supplementary materials[48].

Data availability

The data that support the findings of this study are available from the corresponding author upon reasonable request. Source data are provided with this paper.

References

1. Nakatsuji, S., Kiyohara, N. & Higo, T. Large anomalous Hall effect in a non-collinear antiferromagnet at room temperature. *Nature* **527**, 212 (2015).
2. Nayak, A. K. et al. Large anomalous Hall effect driven by a non-vanishing Berry curvature in the noncolinear antiferromagnet Mn_3Ge. *Sci. Adv.* **2**, e1501870 (2016).
3. Tomiyoshi, S. & Yamaguchi, Y. Magnetic structure and weak ferromagnetism of Mn_3Sn studied by polarized neutron diffraction. *J. Phys. Soc. Jpn.* **51**, 2478 (1982).
4. Li, X. et al. Anomalous Nernst and Righi-Leduc effects in Mn_3Sn: Berry curvature and entropy flow. *Phys. Rev. Lett.* **119**, 056601 (2017).
5. Ikhlas, M. et al. Large anomalous Nernst effect at room temperature in a chiral antiferromagnet. *Nat. Phys.* **13**, 1085 (2017).
6. Xu, L. et al. Finite-temperature violation of the anomalous transverse Wiedemann-Franz law. *Sci. Adv.* **6**, eaaz3522 (2020).
7. Li, X., Zhu, Z. & Behnia, K. A monomaterial Nernst thermopile with hermaphroditic legs. *Adv. Mater.* **33**, 2100751 (2021).
8. Yang, H. et al. Topological Weyl semimetals in the chiral antiferromagnetic materials Mn_3Ge and Mn_3Sn. *N. J. Phys.* **19**, 015008 (2017).
9. Kuroda, K. et al. Evidence for magnetic Weyl fermions in a correlated metal. *Nat. Mater.* **16**, 1090 (2017).
10. Liu, J. & Balents, L. Anomalous Hall effect and topological defects in antiferromagnetic Weyl semimetals: Mn_3Sn/Ge. *Phys. Rev. Lett.* **119**, 087202 (2017).
11. Miwa, S. et al. Giant effective damping of octupole oscillation in an antiferromagnetic Weyl semimetal. *Small Sci.* **1**, 2000062 (2021).
12. Suzuki, M.-T., Koretsune, T., Ochi, M. & Arita, R. Cluster multipole theory for anomalous Hall effect in antiferromagnets. *Phys. Rev. B* **95**, 094406 (2017).
13. Zelenskiy, A., Monchesky, T. L., Plumer, M. L. & Southern, B. W. Anisotropic magnetic interactions in hexagonal *AB*-stacked kagome lattice structures: Application to Mn_3X (X = Ge, Sn, Ga) compounds. *Phys. Rev. B* **103**, 144401 (2021).
14. Park, P. et al. Magnetic excitations in non-collinear antiferromagnetic Weyl semimetal Mn_3Sn. *npj Quantum Mater.* **3**, 63 (2018).
15. Tsai, H. et al. Electrical manipulation of a topological antiferromagnetic state. *Nature* **580**, 608 (2020).
16. Baltz, V. et al. Antiferromagnetic spintronics. *Rev. Mod. Phys.* **90**, 015005 (2018).
17. Šmejkal, L., Mokrousov, Y., Yan, B. & MacDonald, A. H. Topological antiferromagnetic spintronics. *Nat. Phys.* **14**, 242 (2018).
18. Kimata, M. et al. Magnetic and magnetic inverse spin Hall effects in a non-collinear antiferromagnet. *Nature* **565**, 627 (2019).
19. Higo, T. et al. Perpendicular full switching of chiral antiferromagnetic order by current. *Nature* **607**, 474 (2022).
20. Ikhlas, M. et al. Piezomagnetic switching of the anomalous Hall effect in an antiferromagnet at room temperature. *Nat. Phys.* **18**, 1086 (2022).
21. Chen, H., Niu, Q. & MacDonald, A. H. Anomalous Hall effect arising from noncollinear antiferromagnetism. *Phys. Rev. Lett.* **112**, 017205 (2014).
22. Borovik-romanov, A. S. Piezomagnetism, linear magnetostriction and magnetooptic effect. *Ferroelectrics* **162**, 153 (1994).
23. Pippard, A. B. *Elements of classical thermodynamics: for advanced students of physics*, https://books.google.fr/books?id=GVhaSQ7eBQoC (Cambridge University Press, 1964).
24. Joule, J. P. On the effects of magnetism upon the dimensions of iron and steel bars. *Sturgeon's. Ann. Electricity* **8**, 219 (1842).
25. Liu, J., Jiang, C. & Xu, H. Giant magnetostrictive materials. *Sci. China Technol. Sci.* **55**, 1319 (2012).
26. Chandrasekhar, B. S. & Fawcett, E. Magnetostriction in metals. *Adv. Phys.* **20**, 775 (1971).
27. Puech, L. et al. High-field magnetostriction in the pseudo-metamagnetic heavy-fermion system $CeRu_2Si_2$. *J. Low. Temp. Phys.* **70**, 237 (1988).
28. Küchler, R. et al. Thermodynamic evidence for valley-dependent density of states in bulk bismuth. *Nat. Mater.* **13**, 461 (2014).
29. Lee, E. W. Magnetostriction and magnetomechanical effects. *Rep. Prog. Phys.* **18**, 184 (1955).
30. Chopra, H. D. & Wuttig, M. Non-joulian magnetostriction. *Nature* **521**, 340 (2015).
31. Ma, H.-Y. et al. Multifunctional antiferromagnetic materials with giant piezomagnetism and noncollinear spin current. *Nat. Commun.* **12**, 2846 (2021).
32. Jaime, M. et al. Piezomagnetism and magnetoelastic memory in uranium dioxide. *Nat. Commun.* **8**, 99 (2017).
33. Birss, R. R. & Anderson, J. C. Linear magnetostriction in antiferromagnetics. *Proc. Phys. Soc.* **81**, 1139 (1963).
34. Alberts, L. & Lee, E. W. Magnetostriction in antiferromagnetic nickel oxide. *Proc. Phys. Soc.* **78**, 728 (1961).
35. Lines, M. E. Elastic properties of magnetic materials. *Phys. Rep.* **55**, 133 (1979).
36. Tavger, B. A. Symmetry of piezomagnetic crystals. *Sov. Phys. Crystallogr* **3**, 341 (1958).
37. Moral, A. D. & Brooks, M. S. S. Field dependence of forced magnetostriction in cubic ferro-, ferri and antiferromagnets. *J. Phys. C: Solid State Phys.* **7**, 2540 (1974).
38. Theuss, F. et al. Strong magnetoelastic coupling in Mn3*X* (*X* = Ge, Sn). *Phys. Rev. B* 105, 174430 (2022).
39. Balents, L. Antichiral order and spin reorientation transitions of triangle-based antiferromagnets. *Phys. Rev. B* **106**, L020403 (2022).
40. Li, X. et al. Free energy of twisting spins in Mn_3Sn. *Phys. Rev. B* **106**, L020402 (2022).
41. Song, Y. et al. The critical role of spin rotation in the giant magnetostriction of $La(Fe,Al)_{13}$. *Sci. China Mater.* **64**, 1238 (2021).
42. Li, X. et al. Momentum-space and real-space Berry curvatures in Mn_3Sn. *SciPost Phys.* **5**, 063 (2018).
43. Ikhlas, M., Tomita, T., and Nakatsuji, S. *Proceedings of the International Conference on Strongly Correlated Electron Systems (SCES2019)*, JPS Conference Proceedings, Vol. 30, https://doi.org/10.7566/JPSCP.30.011177 (Journal of the Physical Society of Japan, 2020)
44. Krén, E., Paitz, J., Zimmer, G. & Zsoldos, E. Study of the magnetic phase transformation in the Mn_3Sn phase. *Phys. B+C.* **80**, 226 (1975).
45. Küchler, R., Bauer, T., Brando, M. & Steglich, F. A compact and miniaturized high resolution capacitance dilatometer for measuring thermal expansion and magnetostriction. *Rev. Sci. Instrum.* **83**, 095102 (2012).
46. Kübler, J. & Felser, C. Non-collinear antiferromagnets and the anomalous Hall effect. *EPL (Europhys. Lett.)* **108**, 67001 (2014).
47. Song, Y. et al. Opposite thermal expansion in isostructural noncollinear antiferromagnetic compounds of Mn_3A (A = Ge and Sn). *Chem. Mater.* **30**, 6236 (2018).
48. See Supplementary Materials for more details (2023)
49. Kurosawa, S. et al. Chiral-anomaly-driven magnetotransport in the correlated weyl magnet Mn_3Sn, https://arxiv.org/abs/2204.00882 (2022).

50. Li, X. et al. Chiral domain walls of Mn_3Sn and their memory. *Nat. Commun.* **10**, 3021 (2019).
51. Kresse, G. & Hafner, J. Ab initio molecular dynamics for liquid metals. *Phys. Rev. B* **47**, 558 (1993).
52. Blöchl, P. E. Projector augmented-wave method. *Phys. Rev. B* **50**, 17953 (1994).
53. Perdew, J. P., Burke, K. & Ernzerhof, M. Generalized gradient approximation made simple. *Phys. Rev. Lett.* **77**, 3865 (1996).
54. Borovik-Romanov, A. S., Grimmer, H., Kenzelmann, M. Magnetic properties, in *International Tables for Crystallography*, https://doi.org/10.1107/97809553602060000904 (Wiley Online Library, 2013).
55. Baruchel, J. et al. Piezomagnetism and domains in MnF_2. *J. Phys. Colloq.* **49**, C8 (1988).
56. Sandlund, L. et al. Magnetostriction, elastic moduli, and coupling factors of composite Terfenol-D. *J. Appl. Phys.* **75**, 5656 (1994).

Acknowledgements

This work was supported by The National Key Research and Development Program of China (Grant No. 2023YFA1609600, 2022YFA1403500), the National Science Foundation of China (Grant No. 12304065, 12004123, 51861135104 and 11574097) and the Fundamental Research Funds for the Central Universities (Grant No. 2019kfyXMBZ071). K. B. was supported by the Agence Nationale de la Recherche (ANR-19-CE30-0014-04). S. J. acknowledges a PhD scholarship by the China Scholarship Council (CSC). L.B. was supported by the NSF CMMT program under Grant No. DMR-2116515.

Author contributions

X.L., Z.Z., and K.B. conceived and designed the study. Q.M. helped by P.N, L.X., J. W., S.J., and H.Z. performed the measurements. J.D. and J.Z. performed the *abinitio* calculations. L.B. carried out a theoretical analysis of the linear magnetostriction. Q.M., X.L., Z.Z., L.B., and K.B. analyzed the data. Q.M., X.L., Z.Z., L.B., and K.B. wrote the manuscript with assistance from all the authors.

Competing interests

The authors declare no competing interests.

Additional information

Supplementary information The online version contains supplementary material available at https://doi.org/10.1038/s41467-024-51268-y.

Correspondence and requests for materials should be addressed to Xiaokang Li, Zengwei Zhu or Kamran Behnia.

Peer review information *Nature Communications* thanks Tomoya Higo, and the other, anonymous, reviewer(s) for their contribution to the peer review of this work. A peer review file is available.

Reprints and permissions information is available at http://www.nature.com/reprints